Solar Energy 263 (2023) 111895

Contents lists available at ScienceDirect

Solar Energy

journal homepage: www.elsevier.com/locate/solener

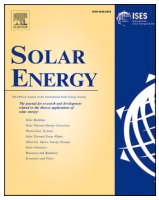

CAELUS: Classification of sky conditions from 1-min time series of global solar irradiance using variability indices and dynamic thresholds

José A. Ruiz-Arias [a,*], Christian A. Gueymard [b]

[a] Universidad de Málaga, Facultad de Ciencias, Física Aplicada I, Campus Teatinos s/n, 29071 Málaga, España
[b] Solar Consulting Services, Colebrook, NH 03576, USA

ARTICLE INFO

Keywords:
Solar irradiance
Sky classification
Variability
Cloudiness
Clear-sky detection
Climate

ABSTRACT

Precise sky classification as a function of cloudiness is desirable or necessary in a variety of applications. CAELUS, a novel classification algorithm that relies on various thresholds to separate all possible sky conditions into six classes, is presented here. It uses global horizontal irradiance (GHI) measurements at 1-min resolution, from which a set of four indices is derived to characterize the magnitude and temporal variability of GHI. The algorithm also requires precise estimates of 1-min GHI under hypothetical cloudless conditions, and the solar zenith angle (limited to a maximum of 85°). Using 1-min GHI measurements from 54 BSRN high-quality radiometric stations, which cover all five primary Köppen-Geiger climate classes, CAELUS is used here to classify their sky conditions. The classification results, including the distribution of sky classes and the transitions between consecutive sky classes, are found consistent with the known characteristics of each primary Köppen-Geiger climate. Moreover, in each climate class, the detection of 1-min cloudless situations is found comparable to that provided by two dedicated and state-of-the-art methods—Reno-Hansen and Bright-Sun.

1. Introduction

Both the amount and variability of incident solar irradiance at the ground determine the solar resource characteristics which, in turn, constraint the design, financing, exploitation, and production management of solar energy applications. Sky conditions can change rapidly, and so does the solar resource, so that any subsequent design, development and management must cope with such variable conditions. For instance, in the context of solar radiation modeling, sky conditions have a direct impact on the expected performance of radiative transfer models and energy production simulation models, whose usage is ubiquitous in solar applications. (These two types of models are referred to as "solar models" in what follows.) In particular, it is common knowledge that the incident irradiance is easier to predict under cloudless conditions than under partly cloudy situations because, among other issues, the passage of dense clouds results in sudden, up or down ramps [28,27,43], which are difficult to capture by conventional solar models. In turn, extreme ramping often occurs because of the cloud enhancement phenomenon [14,26], whose modelling is specially challenging [23].

The identification of the specific sky situations under which a solar model is operating should help isolate its possible weaknesses and facilitate the development of efficient strategies for its ulterior improvement. This is especially relevant for the energy simulation of solar systems using planar photovoltaic (PV) generators (which respond instantaneously to changes in the incident global irradiance), focusing thermal collectors (which are driven by the more variable direct irradiance, but also have substantial thermal inertia), or concentrating PV collectors (which are driven by direct irradiance with no thermal inertia). Unfortunately, sky conditions evolve continuously—and often rapidly—from one situation to the next, which hinders the precise definition of prevailing sky conditions and, by way of consequence, also makes the evaluation of model performance difficult at high frequency. The reduction of such continuous variations into a discrete set of well-defined sky situations, or sky classes, is desirable because it would simplify and accelerate the analysis process [6]. However, although the distinction between a cloudless, a partly cloudy, and an overcast sky appears conspicuous from a qualitative standpoint, it is not so in quantitative terms. The quantification is difficult because of the continuous and relatively fast transitions between sky states. These transitional instances constitute "gray zones" in a high-resolution time series.

The idea of separating sky conditions into classes is not

* Corresponding author.
E-mail address: jararias@uma.es (J.A. Ruiz-Arias).

https://doi.org/10.1016/j.solener.2023.111895
Received 13 May 2023; Received in revised form 30 June 2023; Accepted 19 July 2023
Available online 12 August 2023

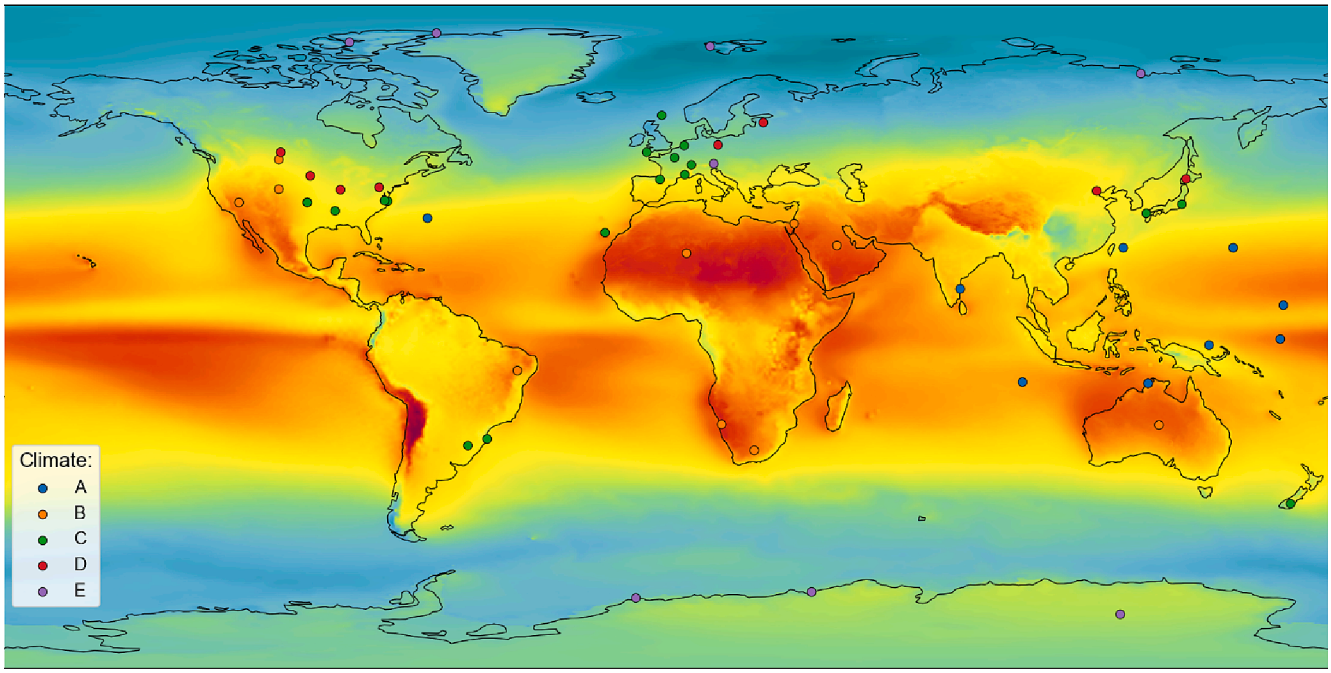

Fig. 1. Location of the BSRN stations (circle markers). The color of the markers indicates the primary Köppen-Geiger climate class at the station location, based on a 1-km grid. The background color shows the mean GHI in the period 2006–2020 from the ECMWF ERA5 reanalysis.

fundamentally new [22,24,25,33,34,38,42]. The studies conducted so far, however, were limited in scope, either regarding the target timescale (e.g., daily or hourly), the number of classes (e.g., cloudless and cloudy), the detection of particularly important situations (e.g., cloud enhancement), the climate representativeness, or the method's validation. These limitations were actually critiqued by Hartmann [21]. Hence, the sky classification task remains still highly challenging, making the development of more robust methodologies all the more desirable.

On a daily timescale, some sky classification appears possible using various definitions of variability indices [7,24], which is helpful to estimate the daily ramping frequency. A relatively similar approach is based on the daily probability of persistence [25]. In parallel, it is also possible, with relatively good overall success, to separate instances of cloudless and cloudy scenes using 1-min time series of global horizontal irradiance (GHI) either alone or in combination with its direct and diffuse components [5,35]. However, this approach only provides a binary classification (cloudless vs. cloudy), which is sufficient only for certain applications, such as the verification of clear–sky solar radiation models [15,40].

In general, there is currently no consensus on the optimal number of sky classes that should be considered because such number generally depends on the intended application, such as for the generation of high-frequency synthetic time series [10,22,34]. As a rule of thumb, the number of classes should be large enough to properly resolve the sky variability, but small enough to objectively separate different classes, and all that should be achieved using classification models with limited complexity. These are practical design constraints of the solution proposed here, which also constitute a main novelty of this contribution. (Some other design constraints are also discussed below, wherever appropriate.).

In general, the state of the sky is primarily characterized by its cloudiness, which directly conditions both the magnitude and the variability of solar irradiance. Reciprocally, an analysis of these quantities is expected to provide critical information about the actual sky conditions, which is the approach ultimately adopted here. Although solar irradiance time series can usually be obtained with a resolution in the range 10–60 min, the impact of irradiance variability on solar systems is better evaluated at higher frequency, such as 1-min time scales, or even higher [1,28,31,38]. For that reason, as well as the relative abundance of long records of 1-min irradiance data over the world, one more design constraint for the method's algorithm is to operate at 1-min temporal resolution.

Furthermore, for easy implementation and application of the classification algorithm, or "classifier", it is desirable that the algorithm be made ultimately dependent on the least possible number of essential variables, which constitutes a challenging design constraint in practice. In particular, a classifier that only uses GHI can be applied to the vast number of radiometric stations that only observe GHI with a single pyranometer. In contrast, if it additionally requires direct normal irradiance (DNI) and/or diffuse horizontal irradiance (DIF), the number of available radiometric stations (typically research-class stations) reduces very significantly. Such stations are costly to install and maintain, and far from being as common as GHI-only stations. Intermediate cases also exist at temporary solar resource stations intended to support solar energy projects, at least during a few months [39]. Such stations are typically equipped with a *rotating shadowband irradiometer* (RSI) to observe both GHI and DIF, but their observations are most often proprietary. Hence, even though approaches that require two or three irradiance components should produce better results than a simpler GHI-only method, the latter has the advantage of being less restrictive, making it usable over a wider range of areas and applications.

In parallel, there are applications in which the multicomponent approach is not even an option to be considered, such as with the ubiquitous solar irradiance separation models [18], because GHI is then the only observed irradiance component available as input for the model. Hence, although a classification method based on the knowledge of two or three irradiance components is presumably advantageous from the accuracy standpoint, exclusive reliance on GHI is the preferred option here, and constitute the last design constraint, because it is better from the perspective of the desired "universal" generalization.

In summary, this work presents a novel sky Classification Algorithm for the Evaluation of cLoUdiness Situations (hence the acronym CAELUS, which is also the name of a Roman god of the sky) that only requires 1-min time series of GHI observations and the support of a clear-sky solar irradiance model. It classifies the sky conditions into 6 classes, from cloudless situations to dense cloudiness, including cloud

enhancement. The classification algorithm is tested worldwide at radiometric stations throughout the primary Köppen-Geiger climate regions [3]. Section 2 describes the database used for the development, testing and benchmarking of the algorithm, and Section 3 describes the algorithm itself. The results are presented in Section 4. The main conclusions of the work are summarized in Section 5.

2. Database

The database used here includes 54 Baseline Surface Radiation Network (BSRN) stations [8] (Fig. 1), with 5 years of data per site, except Petrolina and Solar Village that only have 4 years of data [37]. The specific years for each site were selected after the quality control (QC) process described in Section 2.1 to maximize the number of valid data points. The database comprises a total of 50,502,967 quality-assured GHI observation instances with 1-min time step and solar zenith angle $\leq 85^{\circ}$. In terms of Köppen-Geiger (KG) climate zones (defined here at 1-km resolution), 10 sites are in equatorial climates (class A), amounting to 18.2% of the data, 10 sites are in arid climates (class B; 18.9% of the data), 18 sites are in temperate climates (class C; 35.5% of the data), 8 sites are in cold climates (class D; 14.9% of the data), and 8 sites are in polar climates (class E; 12.5% of the data).

2.1. Quality control process

The observational database has first been subjected to a stringent QC protocol consisting in a suite of tests, such that if a data point does not pass any test, it is flagged and dropped out from subsequent analyses. The first four tests were originally proposed for downwelling shortwave irradiance measurements made at BSRN stations [32], and do require knowledge of the three independent radiation components:

1. Physically possible limits

$$-4\,\mathrm{W\,m^{-2}} \leq G_h \leq 1.5E_{0n}\cos^{1.2}\theta_z + 100\,\mathrm{W\,m^{-2}}$$

$$-4\,\mathrm{W\,m^{-2}} \leq D_h \leq 0.95E_{0n}\cos^{1.2}\theta_z + 50\,\mathrm{W\,m^{-2}}$$

$$-4\,\mathrm{W\,m^{-2}} \leq B_n \leq E_{0n}$$

2. Extremely rare limits

$$-2\,\mathrm{W\,m^{-2}} \leq G_h \leq 1.2E_{0n}\cos^{1.2}\theta_z + 50\,\mathrm{W\,m^{-2}}$$

$$-2 \leq D_h \leq 0.75E_{0n}\cos^{1.2}\theta_z + 30\,\mathrm{W\,m^{-2}}$$

$$-2\,\mathrm{W\,m^{-2}} \leq B_n \leq 0.95E_{0n}\cos^{0.2}\theta_z + 10\,\mathrm{W\,m^{-2}}$$

3. Closure limits

$$|C_R - 1| \leq 0.08, \text{ when } G_h > 50 \text{ and } \theta_z \leq 75^{\circ}$$

$$|C_R - 1| \leq 0.15, \text{ when } G_h > 50 \text{ and } 75^{\circ} < \theta_z < 93^{\circ}$$

4. K-index limits

$$K_T < 1.35, \text{ when } G_h > 50\,\mathrm{W\,m^{-2}}$$

$$K_n < \left(0.03z + 1100\,\mathrm{W\,m^{-2}}\right)/E_{0n}, \text{ when } G_h > 50\,\mathrm{W\,m^{-2}}$$

$$K < 1.10, \text{ when } G_h > 50\,\mathrm{W\,m^{-2}} \text{ and } \theta_z \geq 75^{\circ}$$

$$K < 1.05, \text{ when } G_h > 50\,\mathrm{W\,m^{-2}} \text{ and } \theta_z < 75^{\circ}$$

$$K_n < K_T, \text{ when } G_h > 50\,\mathrm{W\,m^{-2}}$$

$$K < 0.96, \text{ when } G_h > 150\,\mathrm{W\,m^{-2}},\ K_T > 0.6 \text{ and } \theta_z < 85^{\circ}$$

where G_h, D_h and B_n represent the measured GHI, DIF, and DNI, respectively. E_{0n} is the extraterrestrial normal solar irradiance obtained from the solar constant [13] after sun-earth distance correction, θ_z is the solar zenith angle calculated at each time step using the high-precision PSA algorithm [4], z is the station elevation in meters above mean sea level, $K_T = G_h/(E_{0n}\cos\theta_z)$ is the clearness index, $K_n = B_n/E_{0n}$ is the direct normal fraction, $K = D_h/G_h$ is the diffuse fraction, and $C_R = G_h/(D_h + B_n\cos\theta_z)$ is the closure ratio.

Two additional tests are also considered here, based on the ongoing work conducted by a group of experts from the International Energy Agency (IEA) PV Power Systems (PVPS) Task 16 [9]. The first test is aimed at detecting potential "log-down" periods when the datalogger fails and continues to report falsely identical readings for a long time. For GHI and DNI, "log-down" periods are considered when there are at least 15 equal consecutive values, whereas the limit of consecutive identical values is increased to 40 for DIF because it naturally varies much less rapidly over time than GHI or DNI. The second additional test is a "clean-up" test that flags "data islands". They are defined as either hourly periods with less than 10 valid minutes (necessary condition because various variability indices would then not be accurate) or days with less than 20% of valid data.

After QC, the database includes observations of GHI to operate the classifier, and also of DIF because it is needed in Section 4.4 to separately operate the Bright-Sun cloud screening algorithm [5].

CAELUS, which is described in Section 3, requires an estimate of the clear-sky global solar irradiance at each time step, which is obtained here from the SPARTA clear-sky solar irradiance model (Ruiz-Arias, 2023, under review). Very similar results are expected if using alternate high-performance models, such as REST2 [16] or McClear [29]. The atmospheric attenuation is evaluated from local estimates of atmospheric pressure, total-column ozone content, total-column water vapor content, aerosol optical depth, aerosol single-scattering albedo, and surface albedo. All these quantities are retrieved from the NASA's MERRA-2 reanalysis [12]. The original hourly values are linearly interpolated to the location of each BSRN site from the MERRA-2's native spatial grid ($0.5^{\circ}\times 0.625^{\circ}$), and to the BSRN time grid using a mean-preserving splines interpolator [36].

3. Classification algorithm

In general, the imputation of sky conditions is necessarily fuzzy because there are no strict rules that can univocally define every sky class. Thus, various methodologies were initially considered before reaching the actual threshold-based classification algorithm described in Section 3.1. The foremost tentative approach consisted in a two-step process in which, first, a *k–means* unsupervised clustering was conducted to separate the entire QC-assured database into 5 sky classes. (More sophisticated clustering algorithms were also evaluated but did not provide significant benefits.) In a second step, machine-learning supervised classifiers (based on random forests and gradient boosting) were trained to predict the sky classes from the same inputs used by the clustering algorithm. These inputs included a comprehensive set of GHI-based variability indices drawn from the literature [2] and computed at multiple time scales. All combined, several tens of predictors were tested. Despite this sophistication, the results were not satisfactory because there were too many unrealistic transitions between consecutive sky classes (e.g., abrupt jumps from cloudless to cloud enhancement conditions). The reason appeared that the clustering algorithm was not properly accounting for the time series autocorrelation. This issue being

Table 1
Information on the 54 stations from the BSRN network used in this work. The KG Class column refers to the primary Köppen-Geiger climate class for each site on a 1-km grid, and *N* refers to the number of quality-assured 1-min time steps considered at each site, limited to solar zenith angles $\leq 85°$.

Acronym	Station	Latitude	Longitude	Elevation (m)	Period	KG Class	*N*
ALE	Alert	82.49	–62.42	127	2009–2013	E	914,908
ASP	Alice Springs	–23.798	133.888	547	2014–2018	B	1,078,033
BER	Bermuda	32.3008	–64.766	8	2008–2012	A	618,927
BIL	Billings	36.605	–97.516	317	2013–2017	C	845,428
BON	Bondville	40.0667	–88.3667	213	2014–2018	D	798,349
BOS	Boulder	40.125	–105.237	1689	2014–2018	B	971,643
CAB	Cabauw	51.9711	4.9267	0	2014–2018	C	1,154,743
CAM	Camborne	50.2167	–5.3167	88	2012–2016	C	729,450
CAR	Carpentras	44.083	5.059	100	2014–2018	C	1,143,414
CLH	Chesapeake Light	36.905	–75.713	37	2011–2015	C	1,037,279
CNR	CENER	42.816	–1.601	471	2014–2018	C	1,105,698
COC	Cocos Island	–12.193	96.835	6	2014–2018	A	1,001,602
DAA	De Aar	–30.6667	23.993	1287	2003, 2004, 2016–2018	B	1,035,196
DAR	Darwin	–12.425	130.891	30	2010–2014	A	1,137,524
DOM	Concordia Station	–75.1	123.383	3233	2014–2018	E	784,980
DRA	Desert Rock	36.626	–116.018	1007	2014–2018	B	1,028,121
DWN	Darwin Met Office	–12.424	130.8925	32	2014–2018	A	1,107,932
E13	Southern Great Plains	36.605	–97.485	318	2013–2017	C	943,898
EUR	Eureka	79.989	–85.9404	85	2007–2011	E	823,864
FLO	Florianopolis	–27.6047	–48.5227	11	2014, 2015, 2017–2019	C	984,686
FPE	Fort Peck	48.3167	–105.1	634	2014–2018	B	765,962
FUA	Fukuoka	33.5822	130.3764	3	2014–2018	C	1,172,187
GCR	Goodwin Creek	34.2547	–89.8729	98	2014–2018	C	803,674
GOB	Gobabeb	–23.5614	15.042	407	2014–2018	B	1,194,666
GVN	Georg von Neumayer	–70.65	–8.25	42	2014–2018	E	767,654
ISH	Ishigakijima	24.3367	124.1644	6	2014–2018	A	1,083,666
IZA	Izaña	28.3093	–16.4993	2373	2014–2018	C	1,099,834
KWA	Kwajalein	8.72	167.731	10	2012–2016	A	418,963
LAU	Lauder	–45.045	169.689	350	2014–2018	C	1,015,564
LER	Lerwick	60.1389	–1.1847	80	2012–2016	C	720,942
LIN	Lindenberg	52.21	14.122	125	2013–2017	D	998,549
LRC	Langley Research Center	37.1038	–76.3872	3	2015–2019	C	1,146,501
MAN	Momote	–2.058	147.425	6	2008–2012	A	1,132,654
MNM	Minamitorishima	24.2883	153.9833	7	2015–2019	A	1,197,280
NAU	Nauru Island	–0.521	166.9167	7	2008–2012	A	947,134
NYA	Ny-Ålesund	78.925	11.93	11	2014–2018	E	1,075,964
PAL	Palaiseau, SIRTA Obs.	48.713	2.208	156	2014–2018	C	1,150,600
PAY	Payerne	46.815	6.944	491	2014–2018	C	1,010,566
PSU	Rock Springs	40.72	–77.9333	376	2014–2018	D	828,361
PTR	Petrolina	–9.068	–40.319	387	2014–2017	B	583,939
REG	Regina	50.205	–104.713	578	2007–2011	D	1,029,212
SAP	Sapporo	43.06	141.3286	17	2015–2019	D	1,164,015
SBO	Sede Boqer	30.8597	34.7794	500	2007–2011	B	1,084,587
SMS	São Martinho da Serra	–29.4428	–53.8231	489	2012–2016	C	645,680
SON	Sonnblick	47.054	12.9577	3109	2014–2018	E	704,678
SOV	Solar Village	24.91	46.41	650	1999–2002	B	949,996
SXF	Sioux Falls	43.73	–96.62	473	2014–2018	D	813,698
SYO	Syowa	–69.005	39.589	18	2014–2018	E	662,123
TAM	Tamanrasset	22.7903	5.5292	1385	2014–2018	B	851,762
TAT	Tateno	36.0581	140.1258	25	2014–2018	C	1,210,422
TIK	Tiksi	71.5862	128.9188	48	2013–2017	E	551,988
TIR	Tiruvallur	13.0923	79.9738	36	2014–2018	A	553,869
TOR	Toravere	58.264	26.461	70	2014–2018	D	1,103,251
XIA	Xianghe	39.754	116.962	32	2007–2011	D	817,351

considered severe, that modelling avenue was abandoned in favor of a more elaborate threshold-based algorithm, which minimizes the risk for unrealistic sky transitions thanks to an experience-based systematic fine tuning of thresholds, as described below.

3.1. Threshold-based classification algorithm

In the threshold-based approach finally adopted here, the sky classification indices, the thresholds that apply to them, as well as both the type and number of sky classes, are defined and refined through experience. In particular, the sky classification algorithm defines 6 sky classes by imposing threshold values to four time-evolving indices that describe the magnitude and variability of GHI. The first key index is the conventional *clear-sky index*, $K_{cs} = G_h/G_{hc}$, where G_{hc} is the modeled clear-sky GHI for the same 1-min period as the measured GHI. Additionally, three specialized indices are introduced to characterize the average and variability of GHI, as described in what follows.

The second key index, K_m, accounts for the magnitude of the average GHI: $K_m = \bar{G}_h/G_{h,CDA}$, where $\bar{G}_h$ is the moving average of GHI over a centered time window of 30 min, and $G_{h,CDA}$ is the hypothetical clear-sky GHI under a clean-and-dry atmosphere (i.e., without water vapor or aerosols). Usage of $G_{h,CDA}$ results from the inadequacy of E_{0n} or G_{hc} for this particular application. Specifically, normalizing $\bar{G}_h$ by $E_{0n}\cos\theta_z$ cannot account for GHI's natural variation with site elevation. Alternatively, normalizing by G_{hc} exposes the results to error propagation from the model's main atmospheric inputs (aerosol optical depth and water vapor), whose bias can be substantial over certain regions. These regional or site-dependent disturbances, related to the normalization of the classification indices, are highly relevant here because the classification method relies on threshold values that separate different sky

Table 2
Classification tests to determine each sky type. The tests are conducted from the top to the bottom row. The sky is of a certain type if the corresponding test is true. The boldface variables are threshold values (provided in Table 3) that apply to the solar zenith angle and the classification indices. The variable named "cloudy" refers to sky situations that are neither CloudEn nor Cloudless or Overcast. The symbol & is the logical AND operator and the symbol | is the logical OR operator.

Sky type	Description	Tests
CloudEn	Cloud enhancement	$(\theta_z < \boldsymbol{\theta}_{z,max}^{\text{cloudEn}})$ & $\left(K_{cs} > \boldsymbol{K}_{cs,min}^{\text{cloudEn}}\right)$ & $\left(K_v > \boldsymbol{K}_{v,min}^{\text{cloudEn}}\right)$ & $(K_{vf} > \boldsymbol{K}_{vf,min}^{\text{cloudEn}})$
Cloudless	Cloudless	$\left(K_m > \boldsymbol{K}_{m,min}^{\text{Cloudless}}\right)$ & $\left(\boldsymbol{K}_{cs,min}^{\text{Cloudless}} < K_{cs} < \boldsymbol{K}_{cs,max}^{\text{Cloudless}}\right)$ & $\left(K_v < \boldsymbol{K}_{v,max}^{\text{Cloudless}}\right)$
Overcast	Overcast	$\left(K_m < \boldsymbol{K}_{m,max}^{\text{Overcast}}\right)$ & $\left(K_v < \boldsymbol{K}_{v,max}^{\text{Overcast}}\right)$
ThinClouds	Thin clouds	cloudy & $\left(K_m > \boldsymbol{K}_{m,min}^{\text{ThinClouds}}\right)$ & $\left(\boldsymbol{K}_{v,min}^{\text{ThinClouds}} \le K_v < \boldsymbol{K}_{v,max}^{\text{ThinClouds}}\right)$
ThickClouds	Thick clouds	cloudy & $\left(K_m < \boldsymbol{K}_{m,max}^{\text{ThickClouds}}\right)$ & $\left(\boldsymbol{K}_{v,min}^{\text{ThickClouds}} \le K_v < \boldsymbol{K}_{v,max}^{\text{ThickClouds}}\right)$
ScatterClouds	Scattered clouds	not (CloudEn | Cloudless | Overcast | ThinClouds | ThickClouds)

Table 3
Threshold values in the classification tests of Table 2 (i.e., boldface variables therein). The threshold variables' superscript in Table 2 refer to the row here.

Sky type	$\theta_{z,max}$	$K_{cs,min}$	$K_{cs,max}$	$K_{m,min}$	$K_{m,max}$	$K_{v,min}$	$K_{v,max}$	$K_{vf,min}$
CloudEn	80°	1.06	–	–	–	0.20	–	0.20
Cloudless, if $\theta_z < 75^\circ$	–	0.85	1.15	0.6	–	–	0.03	–
Cloudless, if $\theta_z \ge 75^\circ$	–	0.80	1.20	0.6	–	–	0.03	–
Overcast	–	–	–	–	0.3	–	0.10	–
ThinClouds	–	–	–	0.5	–	0.03	0.08	–
ThickClouds	–	–	–	–	0.4	0.04	0.16	–

situations. Thus, the algorithm is highly sensitive to small changes in the indices when they are close to a threshold value, which constitutes a drawback of this classification approach. After thorough testing of different other possibilities at many sites, $G_{h,CDA}$ was found a more appropriate normalization factor.

To quantify the temporal variability in GHI, a third index, K_v, is defined as the *moving sum* of

$$\Delta g = \frac{\left|g_{h,t+1} - g_{h,t}\right|}{\Delta t} \tag{1}$$

over a centered time window of width Δt, where the normalization factor Δt is in seconds, and $g_h = G_h - \bar{G}_h$. As with K_m, the window duration is $\Delta t = 30$ min. Note that g_h simply represents the deviation of the 1-min G_h from the moving-averaged signal $\bar{G}_h$. Hence, Δg gauges the magnitude of the overall variability of these deviations, with a specific focus on the ramps between consecutive g_h values separated by a Δt time interval. Note also that the time window used in the evaluation of both K_m and K_v is chosen centered because the value so obtained is deemed more representative of the actual conditions around the corresponding time step. (In the particular case of real-time applications, the time window is rather defined as the latest 30 min.).

GHI's variability is a critical source of information for the classifier and is often a highly dynamic quantity. For that reason, the very short-term variability in GHI cannot be just described with K_v at its nominal 30-min timescale. Hence, a fourth index, K_{vf}, is used to define the "fine-scale" variability at 10-min resolution. It is defined from Eq. (1) just as K_v, but now using a shorter time window, $\Delta t = 10$ min. Finally, a "daytime" filter is added to prevent the sky classification whenever $\theta_z \ge 85^\circ$.

Based on the previous indices, six sky classes are defined according to the tests described in Table 2, where the threshold values (minimum or maximum) depend on solar zenith angle and specific limits of the irradiance indices, as provided in Table 3. Note that, for the Cloudless type, different coefficients are obtained depending on whether θ_z is below or above 75°. This is mostly because pyranometers are affected by cosine errors caused by the direct beam component under clear conditions; such errors typically increase substantially for $\theta_z > 75^\circ$ [17,20], and also because the indices become more sensitive to small errors (and are thus less reliable) under low-sun situations.

The name of each sky type refers to its expected prevailing sky situation and is thus self-describing. Hence, mostly cloudless situations are expected within the Cloudless sky type. Likewise, mostly overcast situations are expected within the Overcast sky type. In parallel, mostly thick, scattered, and thin clouds are expected within the ThickClouds, ScatterClouds, and ThinClouds sky types, respectively, whereas mostly cloud-enhancement situations are expected within the CloudEn sky type. As highlighted above, however, there are no strict rules that univocally define these classes. Thus, this self-describing naming convention is somewhat fuzzy. This means that, for instance, the ScatterClouds sky type can also include situations that may not actually be exclusively made of scattered clouds, even though most of them can be expected to be scattered clouds. The same comments hold for the other five sky classes.

3.2. Post-threshold filters

In addition to the threshold-based classification described in Table 2, some filters have been implemented to remove various anomalous situations that might arise in case of incorrect classification. In particular, spurious spikes may appear when periods of less than 15 min of a certain sky type are flanked on both sides by sky types of length longer than 15 min. If the spurious spike is not CloudEn and is flanked by either ThickClouds or ScatterClouds on both sides, the spurious spike is set to ThickClouds or ScatterClouds, respectively. If the spurious spike is classified as ThinClouds (Cloudless) and is flanked by Cloudless (ThinClouds) on both sides, it is set to Cloudless (ThinClouds).

Because the ScatterClouds sky type is defined as those situations that are not of any other sky type (which is why it is defined in the last row of Table 2), it also requires some additional filtering. In particular, all ScatterClouds sky patches that are longer than 25 min and shorter than 35 min, and that are flanked by ThinClouds on both sides, are set as ThinClouds unless these four conditions are met: $\theta_z < 70^\circ$, $K_m > 0.7$, $K_v > 0.1$, and $k_v > 0.9$, where k_v is the moving average of K_v over a centered time window of 30 min and normalized by the maximum K_v over that same moving window. Stated differently, k_v is a normalized version of K_v.

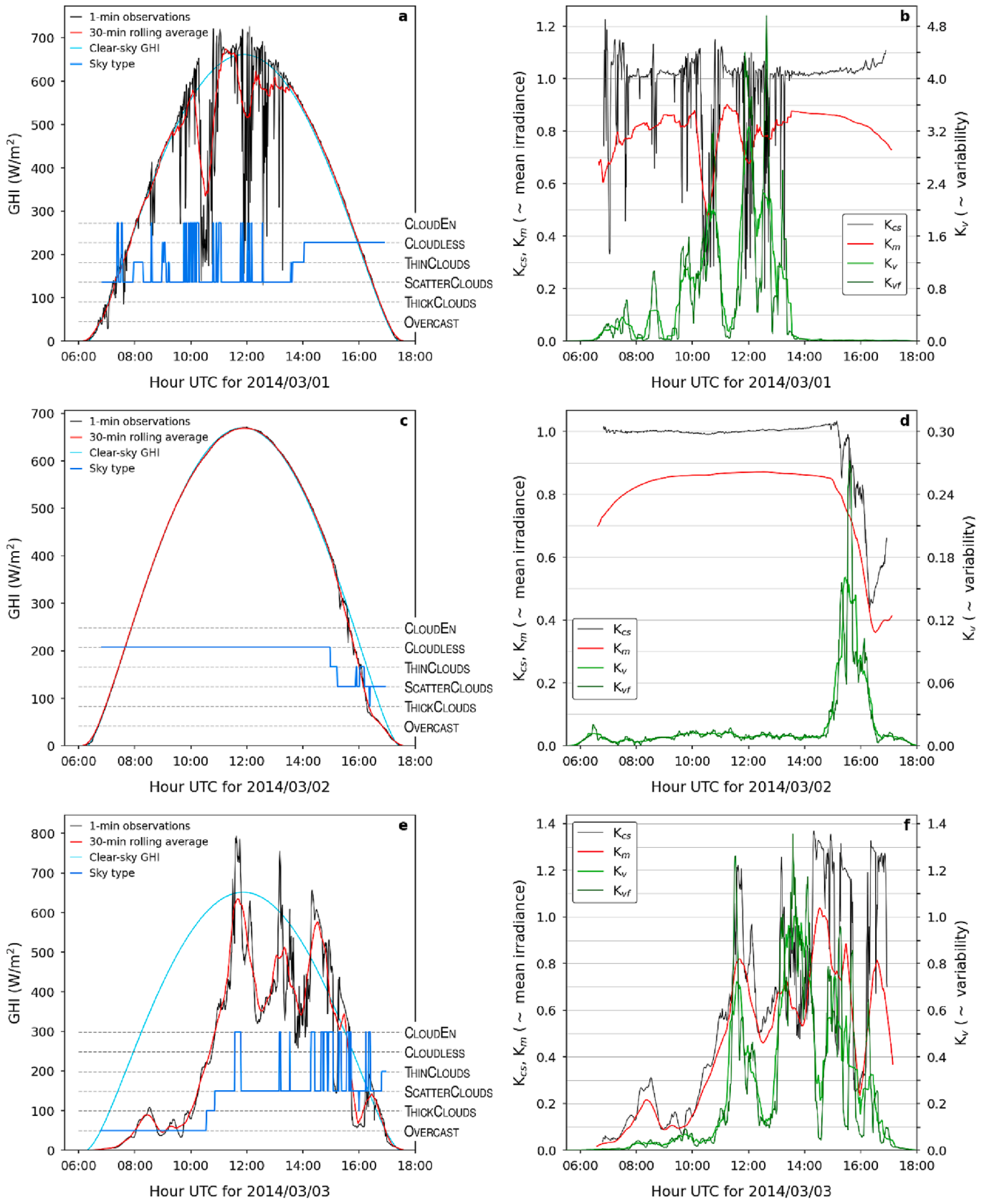

Fig. 2. Example time series of GHI observations, clear-sky GHI, solar irradiance indices, and detected sky classes for 1–3 March 2014 at the BSRN station of Carpentras, France.

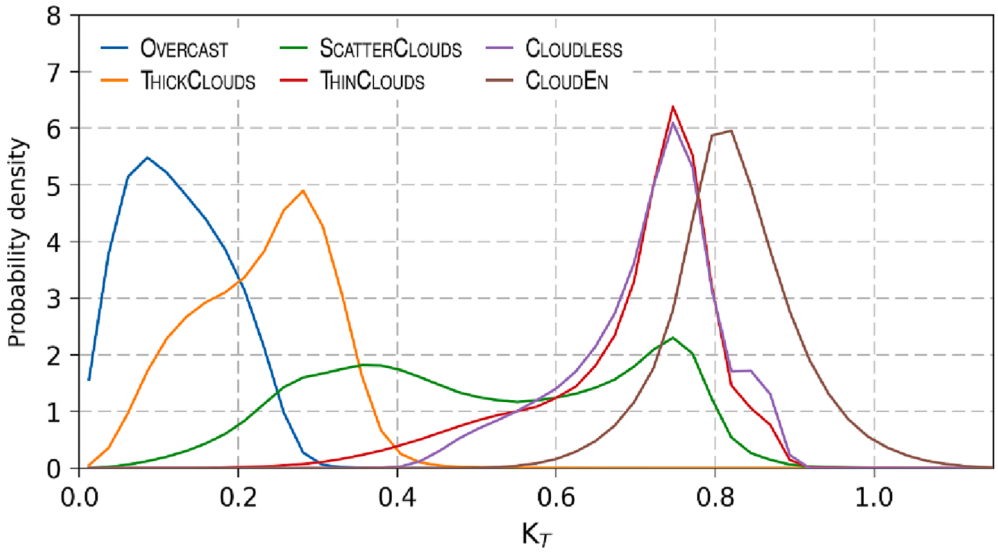

Fig. 3. Probability density of K_T by sky type for all data from the stations under Köppen-Geiger climate C combined. The results for other climates are similar.

4. Results and clear-sky benchmarking

The sky classification results obtained with CAELUS cannot be validated per se because there is no suitable reference to that aim. Even observations from fish-eye sky cameras (which are rarely available) would not be a definite and unambiguous reference source for strict quantitative validation. Under this severe limitation, the approach taken here considers a number of diagnostic results that attempt to demonstrate both the coherence and consistency of the sky classification results, mostly at qualitative level, but also quantitatively as discussed in Section 4.4. Exemplary results are presented in what follows, starting with a showcase of the classifier's working principles.

Fig. 2 shows the case of three consecutive days featuring various sky conditions at Carpentras, southern France. On 1 March 2014, the time series of 1-min GHI observations (Fig. 2a) suggests a morning sky with optically thin passing clouds that progressively turn into a sky with thicker and more variable clouds during the afternoon, eventually producing cloud enhancements. Afterwards, the sky becomes cloudless. The mean GHI and variability indices reflect all these different situations throughout the day (Fig. 2b). In particular, K_{cs} and K_m drop in the presence of clouds, and remain high otherwise, thus helping to discern whether clouds are interfering with GHI or not. In parallel, the K_v and K_{vf} variability indices provide additional information from which it is possible to infer some cloud properties. In this case, for instance, the combination of high variability and high K_{cs} is key to detect cloud enhancements. Later in the afternoon, when the sky becomes cloudless, the variability vanishes while both K_m and K_{cs} remain high, indicating an absence of clouds in the sky—or at least an absence of clouds that would *radiatively* affect the irradiance field in a significant way. All these situations are highlighted by the blue signal in Fig. 2a, which shows the multiple sky classes detected by the algorithm throughout the day.

On 2 March 2014, the sky is cloudless during most of the day (Fig. 2c). During early evening, however, some variability in GHI seems to be induced by light clouds. That is effectively sensed by the K_v and K_{vf} indices (Fig. 2d), and is flagged as ThinClouds and then ScatterClouds. The next day, GHI is very low in the morning, signaling the presence of optically thick clouds (Fig. 2e). This is confirmed by the low GHI variability, as detected by K_v and K_{vf}, and by the small values of K_m and K_{cs} (Fig. 2f). From 10:00 onwards, clouds become thinner and more variable. According to the sky classifier, the sky goes from Overcast during morning to ScatterClouds and CloudEn afterwards.

Another methodological aspect is that a proper evaluation of the different sky classes is only possible if the ideal clear-sky GHI, GHI_{cs}, is accurately predicted. A significant bias in the GHI_{cs} estimate can lead to misclassified conditions. To prevent it as much as possible, a high-performance GHI_{cs} model is necessary (e.g., SPARTA or REST2), and must be operated at least from daily–resolution inputs of aerosol optical depth (AOD) and precipitable water, such as those provided by the MERRA-2 or CAMS reanalysis models. Nevertheless, a potential difficulty here is that their AOD predictions are typically affected by more or less substantial bias, either at local [41] or regional scale [19], which in turn can affect the GHI_{cs} estimates because of error propagation. It is anticipated that future releases of global AOD databases will have less bias, thus resulting in more accurate GHI_{cs} estimates.

A remarkable feature of the classification method is that the sky classes can overlap substantially in terms of K_T (when $K_T \gtrsim 0.5$, most particularly) but can still be univocally classified in terms of ScatterClouds, ThinClouds, Cloudless, or CloudEn classes (Fig. 3). This stresses two important features: (i) the critical role of the variability indices in those cases, since K_T alone cannot differentiate them with confidence (e.g., the ThinClouds and Cloudless classes are similar from the K_T viewpoint but can be separated based on their respective range of variability, as shown in Table 3), and (ii) the strength of the present multi-threshold method in comparison with simplistic schemes that just use sharp K_T thresholds for separation. For instance, a popular trinary sky classification (overcast, partly cloudy, and cloudless) uses dual K_T seams fixed at either 0.35 and 0.65 [11] or 0.24 and 0.50 [30]. In comparison with Fig. 3, it is obvious that such schemes cannot be reliable in practice.

4.1. Sky classification in K–K_T space

The distribution of observations in K–K_T space is strongly determined by the sky conditions during each 1-min period [18]. For instance, under overcast skies, K_T is small and DNI approaches zero, thus K approaches 1. Conversely, under cloudless situations, K_T is large while K is small because DNI is normally much higher than DIF (except, potentially, for exceptionally turbid situations). In the presence of cloud enhancements, K_T is even greater than under cloudless skies but combines with K values that are not necessarily small. In summary, the different sky conditions are expected to be clustered over different regions in K–K_T space. This is precisely what Fig. 4 confirms. It displays the distribution of observations segregated by both sky class and KG climate class. (Each of the latter combines the data from all sites in that specific class.).

The Overcast and ThickClouds sky classes spread over the region characterized by low K_T and high K, with the highest concentration of

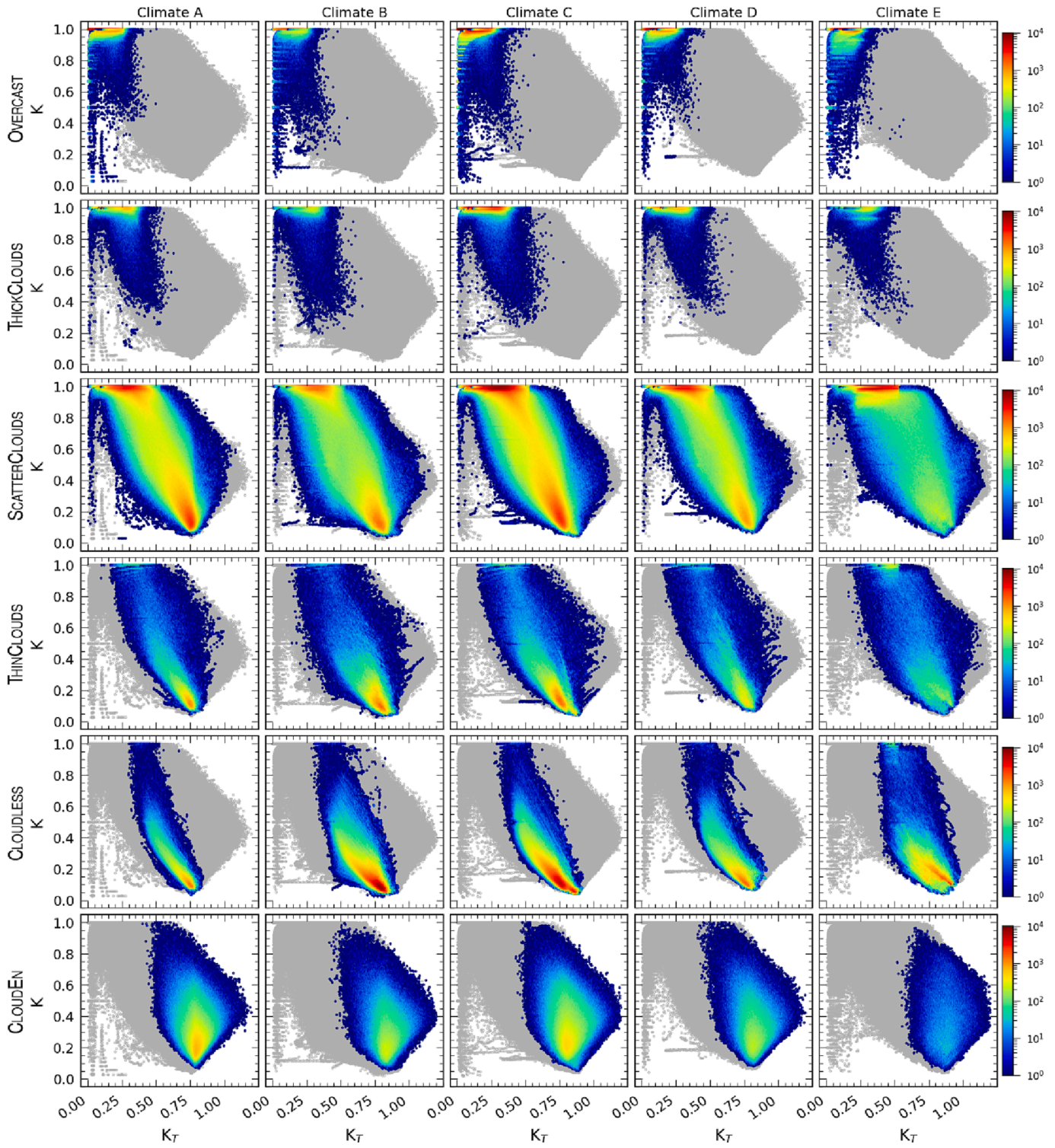

Fig. 4. Distribution of observations in K–K_T space by sky type (each row) and Köppen-Geiger climate class (each column). The corresponding site data are all combined for each climate. The color shows the number density of points. The gray markers show the distribution of all observations, and are used as a relative reference for the distribution of points in each sky class.

points occurring for $K \approx 1$, as expected. The large variety of cloudy situations anticipated within the ScatterClouds class is evidenced by the wide spread of points, almost covering the entire K–K_T space. Interestingly, the distribution of those points also shows the two important modes in the low-K_T–high-K and high-K_T–low-K regions, which have been described in the literature; see, e.g., Fig. 1 of Gueymard and Ruiz-Arias [18].

For both ThinClouds and Cloudless sky types, the greater concentration of points is for high K_T and low K values. However, there are still some situations in which the diffuse fraction can be high, especially in the presence of cirrus clouds, or under cloudless turbid skies. Finally, the observations that are classified within the CloudEn class (i.e., cloud enhancements) spread mostly around high K_T values, greater than those typically found in the Cloudless type, as expected.

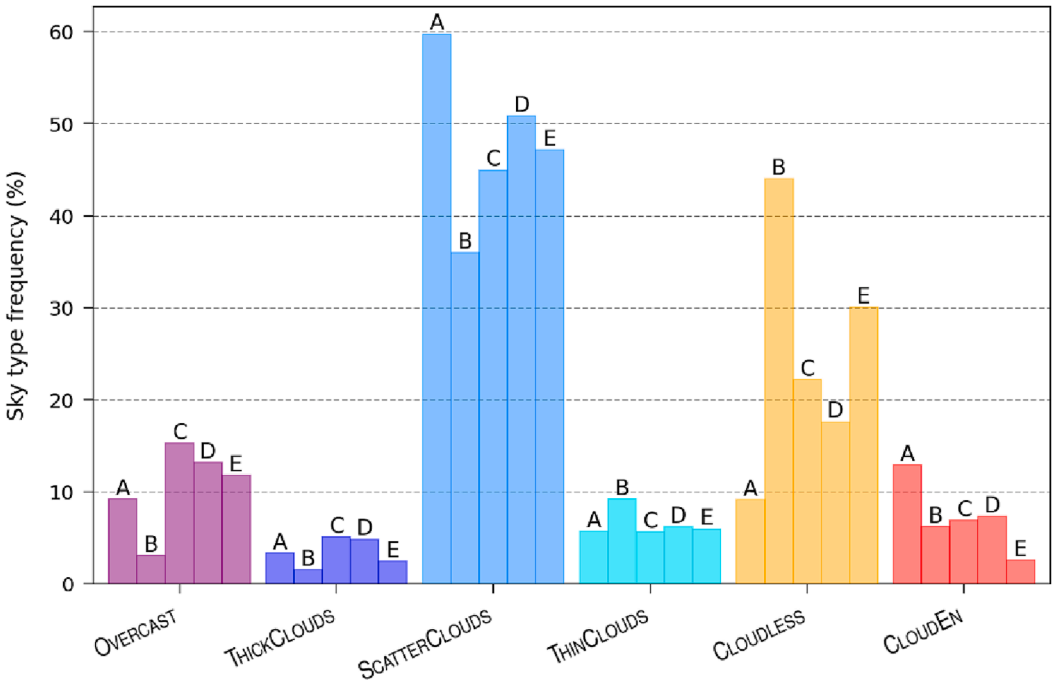

Fig. 5. Relative frequency distribution of sky types for each climate. The label above each bar indicates the climate type.

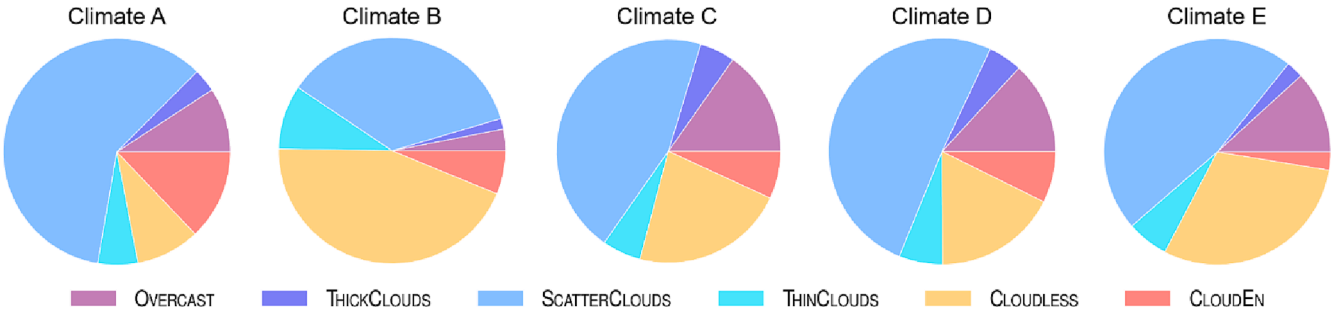

Fig. 6. Relative frequency distribution of sky types for each climate class.

4.2. Frequency distribution of sky types

The distribution of observations in K–K_T space (Fig. 4) does not show too many differences between climates, which could have been anticipated to some extent. However, these differences become evident when comparing the relative frequency distributions of the six sky types (Fig. 5). In particular, the equatorial climate (KG type A) has the highest rate of scattered clouds and cloud enhancements, as expected from the known prevalence of convective clouds near the equatorial belt and the relative proximity of this climate's sites to coastal areas (cf. Table 1 and Fig. 1). At the other extreme, the arid climate (type B) presents the smallest prevalence of overcast skies, thick clouds, and scattered clouds, and the highest prevalence of both thin clouds and cloudless skies. This is consistent with the facts that (i) the low atmospheric humidity over arid regions is conducive to low cloudiness, and that (ii) consequently, these regions typically have the highest solar resource. Interestingly, the present results also show that both temperate and cold climates (types C and D, respectively) are quite similar in terms of sky-type distribution. They present the highest prevalence of overcast situations and thick clouds, with also a significant fraction of scattered clouds (nearly ≈45% and ≈50%, respectively). At the seven polar sites (KG type E) evaluated here, a significant fraction of cloudy skies (>65%) combines with a large fraction of cloudless situations (≈30%) and few cloud enhancements (less than5%). Overall, these results are quite consistent with the expectations for each climate zone, thus suggesting that this sky classification is robust in a climatic sense.

Fig. 6 contains the same information as Fig. 5, but arranged in a different way. Whereas the main segregation was in terms of sky type in the case of Fig. 5, it is in terms of climate class in Fig. 6. The similitude of the overall sky classification between climate classes C and D is clearly visible. Moreover, the contrasting frequencies of ScatterClouds and Cloudless between classes A and B is remarkably obvious in Fig. 6.

4.3. Sky type transition frequency by climate

An important feature of CAELUS is that it is able to provide a realistic chronological succession of sky classes. For instance, in nature, it is not physically possible that a cloudless sky transforms into an overcast sky in just a few minutes, and thus this abrupt transition should not occur in the classifier's results. Fig. 7 analyzes the relative frequency of transitions between consecutive observation time steps. The transitions that are not shown have a relative frequency less than 0.4% and are deemed negligible. The remaining transitions, most of which occur frequently, are physically plausible. For instance, the transition path from the Overcast type to the Cloudless class should go through ThickClouds, then ScatterClouds, and then ThinClouds, or maybe directly through Cloudless via ScatterClouds, but never directly from Overcast to Cloudless. As expected, the latter path never happens (or happens with a negligible

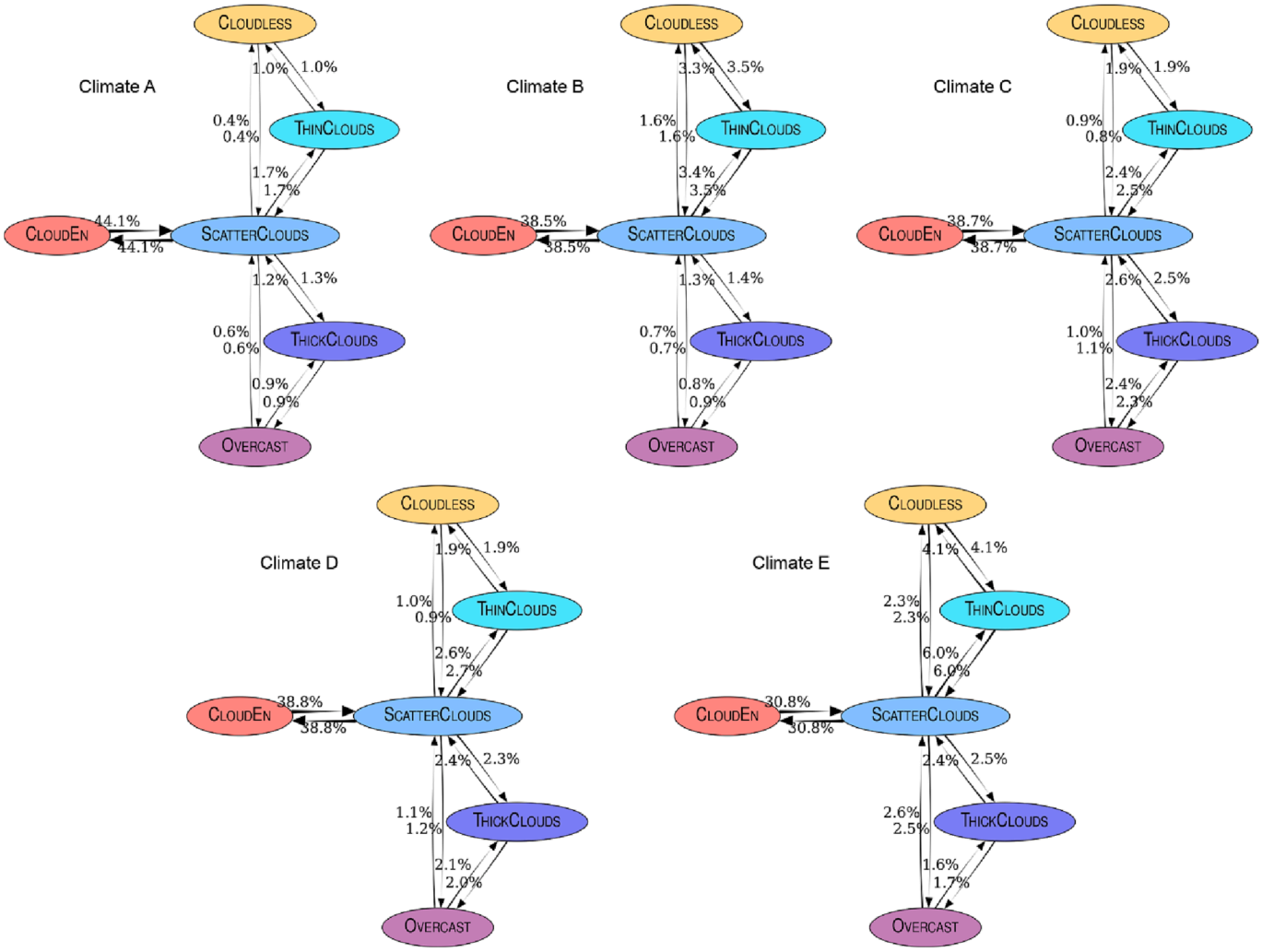

Fig. 7. Frequency of sky type transitions by climate class. The nodes represent each sky type. The arrows are the transitions between sky types, with the relative frequency shown near each transition arrow. The missing transitions between nodes (e.g., between cloud enhancement and cloudless skies) are deemed negligible because their relative frequency is less than 0.4%.

frequency). The same comments apply to other unlikely transition paths, such as from Overcast to ThinClouds, or from ThinClouds to CloudEn.

The transition with the highest rate for all climates is that between CloudEn and ScatterClouds (from a minimum of 30.8% for climate E to a maximum of 44.1% for climate A). This result is expected because these two sky types are precisely characterized by a high variability of solar irradiance. For all climates, except for climate E, the change from Overcast to ScatterClouds, or vice versa, occurs most often through the ThickClouds intermediate step. Likewise, but now for all climates, the change from ScatterClouds to Cloudless, or vice versa, occurs most often through ThinClouds. All these transition paths are physically sound.

4.4. Clear-sky benchmark

As a final test, the cloudless conditions detected by CAELUS are compared against the results of two specialized cloud–screening algorithms, namely, Reno-Hansen [35] and Bright-Sun [5]. The former only requires 1-min observations of GHI, whereas the latter also requires DNI and/or DIF. Hence, the Reno-Hansen method is deemed a method of the same category (i.e., minimal input requirements) as CAELUS; in contrast, Bright-Sun is expected to produce more reliable results. For this reason, the latter is used here as a control reference to evaluate the results of CAELUS, which are also compared against the Reno-Hansen results. All the three methods depend on 1-min predictions of clear-sky irradiance. To make things perfectly comparable, the same SPARTA model is used in all cases.

Fig. 8 displays scatterplots that compare the observed GHI under situations classified as cloudless to the modelled GHI_{cs}, using each of the three clear-sky detection methods mentioned above, at all the 54 BSRN stations segregated into the five primary KG climate classes. Overall, the results of the three methods are similar, although some differences are immediately noticeable. For climate classes B and E, for instance, the scatter around the diagonal is larger with Bright-Sun. This suggests that either the method filters out less cloud-impacted situations than both Reno-Hansen and CAELUS, or that it is more tolerant than the two other algorithms whenever the observed GHI differs by more than ≈5% from the modeled GHI_{cs}, thus increasing the frequency of reported clear-sky situations. (As discussed in Section 3.1, CAELUS relies on index K_m to attenuate the issues that surface when the clear-sky criterion is based solely on the comparison between the observed GHI and the modelled GHI_{cs}; hence, it could well be that the clear-sky detection obtained by CAELUS is actually more rigorous than that of the reference assumed here, Bright-Sun.).

It is also observed that, under low irradiance values (most likely coincidentally with low-sun conditions), Reno-Hansen is more permissive than Bright-Sun at detecting cloudless instances, whereas the opposite occurs with the CAELUS Cloudless sky type. This situation is quantitatively evidenced in the contingency tables detailed in Table 4. They

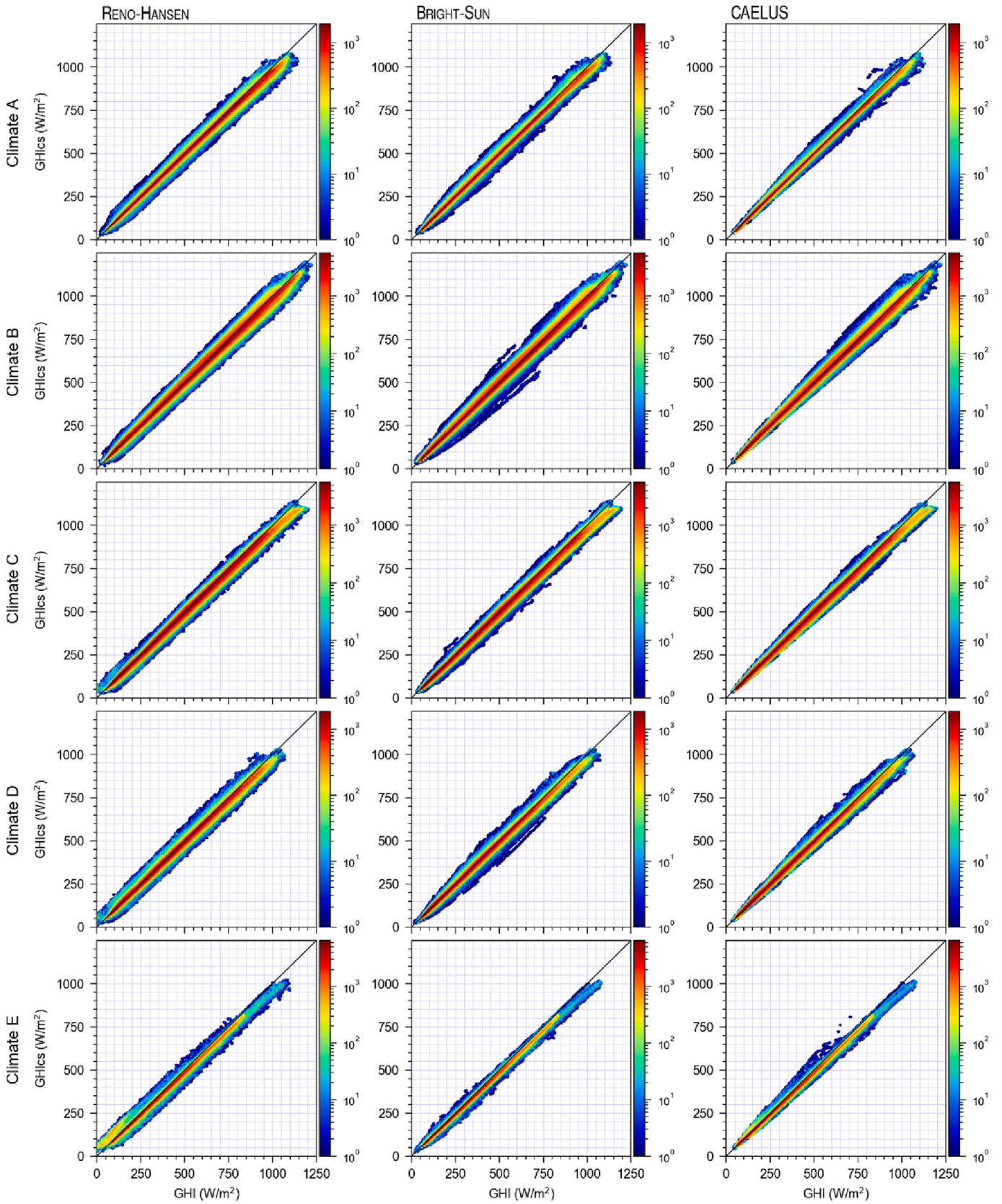

Fig. 8. Density plots of observed GHI vs. modelled clear-sky GHI (GHI_{cs}) under cloudless conditions for each climate (rows). The cloudless conditions are determined alternatively with the RENO-HANSEN algorithm (left column of panels), the BRIGHT-SUN algorithm (middle column), and the CLOUDLESS sky type of the sky classifier (right column). The colors represent the number density of samples.

Table 4
Binary contingency tables of both the Reno-Hansen and the CAELUS Cloudless sky type results compared to the Bright-Sun method for each climate. In all cases, **True** means that a cloudless sky is detected, and **False** otherwise. The figures are in percent of all 1-min cases.

		Climate A Bright-Sun		Climate B Bright-Sun		Climate C Bright-Sun		Climate D Bright-Sun		Climate E Bright-Sun	
		False	True	False	True	False	True	False	True	False	True
Reno-Hansen	False	81.2	2.1	43.8	2.9	70.5	1.6	75.1	1.5	65.6	1.1
	True	6.4	10.2	9.7	43.6	6.6	21.3	7.4	15.9	8.8	24.5
CAELUS	False	86.8	3.9	49.8	6.2	75.0	2.8	80.1	2.3	69.4	0.5
	True	0.8	8.4	3.7	40.3	2.1	20.1	2.4	15.2	5.0	25.1

show that, for all climates (except climate E), CAELUS produces more *misses* (i.e., no cloudless sky is detected, although it is cloudless according to Bright-Sun) than Reno-Hansen, but less *false alarms* (i.e., a cloudless sky is detected, although it is not cloudless according to Bright-Sun). For instance, Reno-Hansen has 1.6% misses in climate C; this is somewhat less than CAELUS, which misses 2.8%. In parallel, Reno-Hansen generates 6.6% of false alarms, more than CAELUS (2.1%). All this means that, under the hypothesis that the Bright–Sun results are correct, there might be inadvertent harmful cloud interference in the results when Reno–Hansen is used to screen cloud-contaminated observations. Conversely, however, the CAELUS Cloudless type might reject some clear-sky instances, which might lead to biased results—especially for low sun elevations or turbid skies. This appears as a relatively minor downside of using a much more general method that can provide results just based on GHI observations. In practice, only the application requirements can determine whether the risk is acceptable or not.

The fact that CAELUS detects less cloudless instances than Reno-Hansen under low-GHI situations, as shown in Fig. 8, is also revealed by its smaller fraction of hits in Table 4 (i.e., a cloudless situation is detected, coincidentally with Bright-Sun). For instance, Reno-Hansen has 21.3% hits for climate C, whereas CAELUS has just 20.1%. This small difference is not necessarily detrimental, however. Indeed, the fraction of cloudless instances detected by CAELUS is always closer to the fraction detected by Bright-Sun. For instance, CAELUS detects that 22.2% of the observations are cloudless in climate C, which is closer to the Bright-Sun results (22.9%) than to those of Reno-Hansen (27.9%).

5. Conclusions

A threshold-based sky classification algorithm, CAELUS, has been presented, using ≈50 million quality-assured data points from 54 high-quality radiometric stations in various climates. The novel algorithm has been found more efficient and reliable than other tentative techniques, such as a 5-class *k–means* unsupervised clustering approach. The proposed method requires 1-min time series of measured GHI and the support of a high-performance clear-sky solar irradiance model to classify the sky conditions into 6 different classes. To that aim, it imposes threshold values onto four custom solar irradiance indices that account for GHI's magnitude and variability. The method also requires the solar zenith angle (up to 85°) and good estimates of the concomitant clear-sky GHI. Although the clear-sky index is a key factor, the classification is also largely dependent on two GHI-derived variability indices. They are essential to demarcate different cloud situations with similar clear-sky index. The thresholds are prescribed based on experience-based trial and error. The sky types broadly represent overcast, thick clouds, scattered clouds, thin clouds, cloudless, and cloud-enhancement situations.

The consistency of the classification results has been assessed by various means. In particular, the clustering of points for the various sky classes over the whole $K{-}K_T$ space was found as expected, and did not show large differences when segregated according to the primary Köppen-Geiger climates. It was also shown that both the overall frequency distribution of sky classes and the transitions between one class to all others are consistent with the expected climatic behavior within each of the five primary Köppen-Geiger climate classes.

The comparison against the state-of-the-art Reno-Hansen and Bright-Sun clear-sky detection algorithms demonstrated that CAELUS is able to consistently provide similar results of clear-sky instances in each of the five climate classes. The differences between the results of these algorithms are likely smaller than their intrinsic uncertainty, which is a combination of the fuzzy definition of sky classes, the empirical methods used in the development of the algorithms, the reliance on imperfect clear-sky irradiance estimates, and the lack of appropriate reference data sources for more elaborate validation.

Precise knowledge of the prevailing sky conditions in the analysis of solar energy systems provides a new tool for potential improvement in the related models and simulation methods. Moreover, it is anticipated that the proposed sky classification method can also find applications in various other fields, such as solar irradiance forecasting or climate-related studies.

6. Data and code availability

The quality-assured data used and developed throughout this research is made publicly available in https://doi.org/10.5281/zenodo.7897639. The dataset is organized as a collection of zipped csv files, one per ground station and per year, that include all the required variables to run CAELUS, plus the sky classification results. The source of observational data is the Baseline Surface Radiation Network (BSRN) data archive, which is publicly available. See download instructions in https://bsrn.awi.de/data.

In addition to the dataset, the Python code developed during this research that implements the CAELUS algorithm is made publicly available in https://github.com/jararias/caelus. It can be used in combination with the previous data to classify the sky situations at all ground sites. See the code repository for usage information.

Declaration of Competing Interest

The authors declare that they have no known competing financial interests or personal relationships that could have appeared to influence the work reported in this paper.

Acknowledgments

This work was supported by the project PID2019-107455RB-C21 funded by MCIN/AEI/ 10.13039/501100011033, the project UMA20-FEDERJA-134 jointly funded by the FEDER 2014-2020 Operative Program and the Consejería de Economía, Conocimiento, Empresas y Universidad of the Junta de Andalucía, and by Solargis s.r.o. through the collaboration agreement 2021-124 with the University of Málaga. The authors would like to thank the scientists and personnel in charge of the BSRN stations for acquiring, processing and kindly sharing their datasets, which have been central to this study. Moreover, the authors acknowledge the scientists and personnel of the Global Modelling and Assimilation Office at NASA Goddard Space Flight Center who provided the MERRA-2 atmospheric data that were advantageously used to calculate the clear-sky solar irradiance at all sites. The University of Málaga/CBUA provided the funding for open access.

References

[1] Adye, K., Pearre, N., Swan, L., 2018. Contrasting distributed and centralized photovoltaic system performance using regionally distributed pyranometers. Sol. Energy 160, 1–9. https://doi.org/10.1016/j.solener.2017.11.042.

[2] Aler, R., Galván, I.M., Ruiz-Arias, J.A., Gueymard, C.A., 2017. Improving the separation of direct and diffuse solar radiation components using machine learning by gradient boosting. Sol. Energy 150, 558–569. https://doi.org/10.1016/j.solener.2017.05.018.

[3] Beck, H.E., Zimmermann, N.E., McVicar, T.R., Vergopolan, N., Berg, A., Wood, E. F., 2018. Present and future Köppen-Geiger climate classification maps at 1-km resolution. Sci. Data 5, 180214. https://doi.org/10.1038/sdata.2018.214.

[4] Blanco, M.J., Milidonis, K., Bonanos, A.M., 2020. Updating the PSA sun position algorithm. Sol. Energy 212, 339–341. https://doi.org/10.1016/j.solener.2020.10.084.

[5] Bright, J.M., Sun, X., Gueymard, C.A., Acord, B., Wang, P., Engerer, N.A., 2020. Bright-Sun: A globally applicable 1-min irradiance clear-sky detection model. Renew. Sustain. Energy Rev. 121, 109706 https://doi.org/10.1016/j.rser.2020.109706.

[6] Chakchak, J., Cetin, N.S., 2021. Investigating the impact of weather parameters selection on the prediction of solar radiation under different genera of cloud cover: A case-study in a subtropical location. Measurement 176, 109159. https://doi.org/10.1016/j.measurement.2021.109159.

[7] Czekalski, D., Chochowski, A., Obstawski, P., 2012. Parameterization of daily solar irradiance variability. Renew. Sustain. Energy Rev. 16, 2461–2467. https://doi.org/10.1016/j.rser.2012.01.069.

[8] Driemel, A., Augustine, J., Behrens, K., Colle, S., Cox, C., Cuevas-Agulló, E., Denn, F.M., Duprat, T., Fukuda, M., Grobe, H., Haeffelin, M., Hodges, G., Hyett, N., Ijima, O., Kallis, A., Knap, W., Kustov, V., Long, C.N., Longenecker, D., Lupi, A., Maturilli, M., Mimouni, M., Ntsangwane, L., Ogihara, H., Olano, X., Olefs, M., Omori, M., Passamani, L., Pereira, E.B., Schmithüsen, H., Schumacher, S., Sieger, R., Tamlyn, J., Vogt, R., Vuilleumier, L., Xia, X., Ohmura, A., König-Langlo, G., 2018. Baseline Surface Radiation Network (BSRN): structure and data description (1992–2017). Earth Syst. Sci. Data 10, 1491–1501. https://doi.org/10.5194/essd-10-1491-2018.

[9] Forstinger, A., Wilbert, S., Kraas, B., Fernández Peruchena, C., Gueymard, C.A., Collino, E., Ruiz-Arias, J.A., Polo Martinez, J., Saint-Drenan, Y.-M., Ronzio, D., Hanrieder, N., Jensen, A.R., Yang, D., 2021. Expert Quality Control of Solar Radiation Ground Data Sets, in: Proceedings of the ISES Solar World Congress 2021. Presented at the ISES Solar World Congress 2021, International Solar Energy Society, Virtual, pp. 1–12. 10.18086/swc.2021.38.02.

[10] Frimane, Â., Soubdhan, T., Bright, J.M., Aggour, M., 2019. Nonparametric Bayesian-based recognition of solar irradiance conditions: Application to the generation of high temporal resolution synthetic solar irradiance data. Sol. Energy 182, 462–479. https://doi.org/10.1016/j.solener.2019.02.052.

[11] García-Rodríguez, A., García-Rodríguez, S., Granados-López, D., Díez-Mediavilla, M., Alonso-Tristán, C., 2022. Extension of PAR Models under Local All-Sky Conditions to Different Climatic Zones. Appl. Sci. 12, 2372. https://doi.org/10.3390/app12052372.

[12] Gelaro, R., McCarty, W., Suárez, M.J., Todling, R., Molod, A., Takacs, L., Randles, C.A., Darmenov, A., Bosilovich, M.G., Reichle, R., Wargan, K., Coy, L., Cullather, R., Draper, C., Akella, S., Buchard, V., Conaty, A., da Silva, A.M., Gu, W., Kim, G.-K., Koster, R., Lucchesi, R., Merkova, D., Nielsen, J.E., Partyka, G., Pawson, S., Putman, W., Rienecker, M., Schubert, S.D., Sienkiewicz, M., Zhao, B., 2017. The Modern-Era Retrospective Analysis for Research and Applications, Version 2 (MERRA-2). J. Clim. 30, 5419–5454. https://doi.org/10.1175/JCLI-D-16-0758.1.

[13] Gueymard, C.A., 2018. A reevaluation of the solar constant based on a 42-year total solar irradiance time series and a reconciliation of spaceborne observations. Sol. Energy 168, 2–9. https://doi.org/10.1016/j.solener.2018.04.001.

[14] Gueymard, C.A., 2017. Cloud and albedo enhancement impacts on solar irradiance using high-frequency measurements from thermopile and photodiode radiometers. Part 1: Impacts on global horizontal irradiance. Sol. Energy 153, 755–765. https://doi.org/10.1016/j.solener.2017.05.004.

[15] Gueymard, C.A., 2012. Clear-sky irradiance predictions for solar resource mapping and large-scale applications: Improved validation methodology and detailed performance analysis of 18 broadband radiative models. Sol. Energy 86, 2145–2169. https://doi.org/10.1016/j.solener.2011.11.011.

[16] Gueymard, C.A., 2008. REST2: High-performance solar radiation model for cloudless-sky irradiance, illuminance, and photosynthetically active radiation – Validation with a benchmark dataset. Sol. Energy 82, 272–285. https://doi.org/10.1016/j.solener.2007.04.008.

[17] Gueymard, C.A., Myers, D.R., 2008. Solar Radiation Measurement: Progress in Radiometry for Improved Modeling. In: Badescu, V. (Ed.), Modeling Solar Radiation at the Earth's Surface: Recent Advances. Springer, Berlin, Heidelberg, pp. 1–27. https://doi.org/10.1007/978-3-540-77455-6_1.

[18] Gueymard, C.A., Ruiz-Arias, J.A., 2016. Extensive worldwide validation and climate sensitivity analysis of direct irradiance predictions from 1-min global irradiance. Sol. Energy 128, 1–30. https://doi.org/10.1016/j.solener.2015.10.010.

[19] Gueymard, C.A., Yang, D., 2020. Worldwide validation of CAMS and MERRA-2 reanalysis aerosol optical depth products using 15 years of AERONET observations. Atmos. Environ. 225, 117216 https://doi.org/10.1016/j.atmosenv.2019.117216.

[20] Habte, A., Sengupta, M., Andreas, A., Wilcox, S., Stoffel, T., 2016. Intercomparison of 51 radiometers for determining global horizontal irradiance and direct normal irradiance measurements. Sol. Energy 133, 372–393. https://doi.org/10.1016/j.solener.2016.03.065.

[21] Hartmann, B., 2020. Comparing various solar irradiance categorization methods – A critique on robustness. Renew. Energy 154, 661–671. https://doi.org/10.1016/j.renene.2020.03.055.

[22] Hofmann, M., Riechelmann, S., Crisosto, C., Mubarak, R., Seckmeyer, G., 2014. Improved Synthesis of Global Irradiance with One-Minute Resolution for PV System Simulations. Int. J. Photoenergy 2014, 1–10. https://doi.org/10.1155/2014/808509.

[23] Hogan, R.J., Fielding, M.D., Barker, H.W., Villefranque, N., Schäfer, S.A.K., 2019. Entrapment: An Important Mechanism to Explain the Shortwave 3D Radiative Effect of Clouds. J. Atmospheric Sci. 2019, 48–66. https://doi.org/10.1175/JAS-D-18-0366.1.

[24] Huang, J., Troccoli, A., Coppin, P., 2014. An analytical comparison of four approaches to modelling the daily variability of solar irradiance using meteorological records. Renew. Energy 72, 195–202. https://doi.org/10.1016/j.renene.2014.07.015.

[25] Kang, B.O., Tam, K.-S., 2013. A new characterization and classification method for daily sky conditions based on ground-based solar irradiance measurement data. Sol. Energy 94, 102–118. https://doi.org/10.1016/j.solener.2013.04.007.

[26] Kreuwel, F.P.M., Knap, W.H., Visser, L.R., van Sark, W.G.J.H.M., Vilà-Guerau de Arellano, J., van Heerwaarden, C.C., 2020. Analysis of high frequency photovoltaic solar energy fluctuations. Sol. Energy 206, 381–389. https://doi.org/10.1016/j.solener.2020.05.093.

[27] Lave, M., Kleissl, J., 2010. Solar variability of four sites across the state of Colorado. Renew. Energy 35, 2867–2873. https://doi.org/10.1016/j.renene.2010.05.013.

[28] Lave, M., Reno, M.J., Broderick, R.J., 2015. Characterizing local high-frequency solar variability and its impact to distribution studies. Sol. Energy 118, 327–337. https://doi.org/10.1016/j.solener.2015.05.028.

[29] Lefèvre, M., Oumbe, A., Blanc, P., Espinar, B., Gschwind, B., Qu, Z., Wald, L., Schroedter-Homscheidt, M., Hoyer-Klick, C., Arola, A., Benedetti, A., Kaiser, J.W., Morcrette, J.-J., 2013. McClear: a new model estimating downwelling solar radiation at ground level in clear-sky conditions. Atmospheric Meas. Tech. 6, 2403–2418. https://doi.org/10.5194/amt-6-2403-2013.

[30] Li, D.H.W., Lau, C.C.S., Lam, J.C., 2004. Standard Skies Classification Using Common Climatic Parameters. J. Sol. Energy Eng. 126, 957–964. https://doi.org/10.1115/1.1740776.

[31] Lohmann, G.M., Monahan, A.H., 2018. Effects of temporal averaging on short-term irradiance variability under mixed sky conditions. Atmospheric Meas. Tech. 11, 3131–3144. https://doi.org/10.5194/amt-11-3131-2018.

[32] Long, C.N., Shi, Y., 2008. An Automated Quality Assessment and Control Algorithm for Surface Radiation Measurements. Open Atmospheric Sci. J. 2, 23–37. https://doi.org/10.2174/1874282300802010023.

[33] Moreno-Tejera, S., Silva-Pérez, M.A., Ramírez-Santigosa, L., Lillo-Bravo, I., 2017. Classification of days according to DNI profiles using clustering techniques. Sol. Energy 146, 319–333. https://doi.org/10.1016/j.solener.2017.02.031.

[34] Perry, M., Troccoli, A., 2017. An approach for generating synthetic fine temporal resolution solar radiation time series from hourly gridded datasets. Meteorol. Z. 26 (3), 265–276.

[35] Reno, M.J., Hansen, C.W., 2016. Identification of periods of clear sky irradiance in time series of GHI measurements. Renew. Energy 90, 520–531. https://doi.org/10.1016/j.renene.2015.12.031.

[36] Ruiz-Arias, J.A., 2022. Mean-preserving interpolation with splines for solar radiation modeling. Sol. Energy 248, 121–127. https://doi.org/10.1016/j.solener.2022.10.038.

[37] Ruiz-Arias, J.A., Gueymard, C.A., 2023. CAELUS: Classification of sky conditions from 1-min time series of global solar irradiance using variability indices and dynamic thresholds (Version v2). Zenodo. https://doi.org/10.5281/zenodo.7897639.

[38] Schroedter-Homscheidt, M., Kosmale, M., Jung, S., Kleissl, J., 2018. Classifying ground-measured 1 minute temporal variability within hourly intervals for direct normal irradiances. Meteorol. Z. 27, 161–179. https://doi.org/10.1127/metz/2018/0875.

[39] Sengupta, M., Habte, A., Wilbert, S., Gueymard, C., Remund, J., 2021. Best Practices Handbook for the Collection and Use of Solar Resource Data for Solar Energy Applications: Third Edition (No. NREL/TP-5D00-77635). 10.2172/1778700.

[40] Sun, X., Bright, J.M., Gueymard, C.A., Bai, X., Acord, B., Wang, P., 2021. Worldwide performance assessment of 95 direct and diffuse clear-sky irradiance models using principal component analysis. Renew. Sustain. Energy Rev. 135, 110087 https://doi.org/10.1016/j.rser.2020.110087.

[41] Sun, X., Yang, D., Gueymard, C.A., Bright, J.M., Wang, P., 2022. Effects of spatial scale of atmospheric reanalysis data on clear-sky surface radiation modeling in tropical climates: A case study for Singapore. Sol. Energy 241, 525–537. https://doi.org/10.1016/j.solener.2022.06.001.

[42] Watanabe, T., Oishi, Y., Nakajima, T.Y., 2016. Characterization of surface solar-irradiance variability using cloud properties based on satellite observations. Sol. Energy 140, 83–92. https://doi.org/10.1016/j.solener.2016.10.049.

[43] Wellby, S.J., Engerer, N.A., 2016. Categorizing the Meteorological Origins of Critical Ramp Events in Collective Photovoltaic Array Output. J. Appl. Meteorol. Climatol. 55, 1323–1344. https://doi.org/10.1175/JAMC-D-15-0107.1.